# 8

#### Research Article

Li-jiao Zhang\* and Ming-gao Li

# Study on hydrogen-induced stress corrosion of 7N01-T4 aluminum alloy for railway vehicles

https://doi.org/10.1515/htmp-2022-0045 received February 12, 2022; accepted June 02, 2022

**Abstract:** 7N01-T4 aluminum alloy is widely applied to high speed train body material attributed to its excellent comprehensive mechanical properties; however, its high sensitivity to hydrogen stress corrosion would seriously restrict its further application. In this study, the hydrogeninduced stress corrosion of the base metal and the joint was investigated under slow strain rate test to ascertain the characteristics and mechanism of hydrogen-induced stress corrosion cracking of aluminum alloy. By applying the cathode potential, the morphology of tensile port was studied. Results show that under the action of tensile stress, the free atomic hydrogen produced in the corrosion process or absorbed hydrogen diffuses along the grain boundary into the crack tip region, weakens the grain boundary and causes hydrogen embrittlement, thus accelerating the crack propagation and fracture. These properties provide a broader prospect for the application of 7N01-T4 aluminum alloy in high-speed train body.

**Keywords:** 7N01-T4 aluminum alloy, high speed train, hydrogen-induced stress corrosion

# 1 Introduction

Aluminum alloy has achieved wide application in the current rail transit field due to its characteristics of lightweight, corrosion resistance, and excellent tensile properties [1,2]. Wide-body of aluminum alloy profile enables its application in high-speed train body to become a current research hotspot [3–5]. Thereinto, high-strength A7N01-T4 aluminum alloy is the key structural material

for high-speed train body, car body, and the most ideal medium strength welding structural material [6]. So it is particularly important to study its operating performance, especially the stress corrosion behavior [7].

In the operating process of A7N01-T4 high-strength aluminum alloy component, stress corrosion has a great impact on its strength and always becomes the main reason for its failure. The main strengthening phase of A7N01 high-strength aluminum alloy is MgZn<sub>2</sub> (η phase). Increasing the content of zinc (Zn) and magnesium (Mg) in the solution limit can greatly improve the strength of the alloy, but its stress corrosion cracking (SCC) resistance will decrease. Therefore, the contradiction between SCC sensitivity and strength is still a major difficulty in the industrial application of A7N01 high-strength aluminum alloy [8,9]. A large number of failure analyses and experimental studies show that stress corrosion is the main failure mode of A7N01 high-strength aluminum alloy welded joint. In view of this problem, many scholars have carried out a series of studies and made remarkable progress. Ma et al. [10] studied the SCC sensitivity of A7N01 friction stir welding joint under hydrogen environment, and found that aluminum alloy FSW joint had a large ductility and tensile strength loss, which was caused by hydrogen infiltration into the grain boundary of aluminum alloy material, resulting in material embrittlement. Shen et al. [11] studied the SCC of a 7N01P-T4 aluminum alloy by using improved unilateral notched tensile specimen, and found that the corrosion crack growth rate of A7N01P-T4 alloy in 3.5% sodium chloride solution was 3 orders of magnitude lower than that of corrosion fatigue crack. Hydrogen embrittlement is the main cause of stress corrosion crack and corrosion fatigue crack propagation [12]. Qi et al. [13] found that hydrogen segregation occurred at the grain boundary of aluminum alloy, which increased cell lattice constant and reduced the average binding energy and interatomic binding force of grain boundary atoms, thus increasing the hydrogen embrittlement sensitivity (IHE) of the alloy. In addition, Akbari et al. deeply researched multicriteria optimization of mechanical properties of aluminum composites reinforced with different reinforcing particles

<sup>\*</sup> Corresponding author: Li-jiao Zhang, Technical Research and Development Department, CRRC Industrial Institute Corporation Limited, Beijing, 100070, China, e-mail: zhanglijiao@crrcgc.cc Ming-gao Li: Technical Research and Development Department, CRRC Industrial Institute Corporation Limited, Beijing, 100070, China

type, and an approach based on TOPSIS method was applied for determining the best compromised solution from the obtained pareto-optimal set [14]. Then, they investigated multi-walled carbon nanotubes/aluminum composite fabrication using friction stir processing through simulation and experiment, showing that the wear resistance and hardness of the produced composites are considerably enhanced compared to the base alloy [15]. Aging degree has great influence on IHE of 7050 aluminum alloy. Under the same hydrogen filling condition, the hydrogen content of the aluminum alloy under the under-aged condition is the largest, the hydrogen embrittlement effect is the most obvious, the over-aged hydrogen content is the lowest, the hydrogen embrittlement effect is the weakest, and the peak age is in the middle.

Based on the above research and research status, this work studied the effect of external hydrogen on SCC of aluminum alloy and the characteristics and mechanism of hydrogen-induced stress corrosion of the base metal and the joint, in order to figure out the corrosion resistance properties of weld and fracture properties of the base metal.

# 2 Experiment and methods

#### 2.1 Materials

The 7N01-T4 aluminum alloy sheet with a thickness of 7 mm was selected and its aging state was natural aging as the base material. The joint form is butt joint, and 7N01-T4 welding joint is prepared by laser-arc composite welding process. The filling metal is ER5356 aluminum alloy welding wire containing 5% Mg. Table 1 lists the chemical composition of aluminum alloy and welding wire.

The equipment used in the laser-arc composite welding process is TruDisk 10002 continuous laser and Transpuls Synergic 4000 welding machine. The welding process is realized by ABB robot arm. The process parameters of laser-arc welding are shown in Table 2, and the laser output wavelength is 1.06  $\mu m$ , spot minimum diameter is 0.4 mm, and focal length is 300 mm. The size of the welding test plate is 320 mm  $\times$  160 mm  $\times$  7 mm (length  $\times$  width  $\times$  thickness), and the welding groove is "v" shaped. The heat source configuration with laser in front and arc in back is used for welding.

#### 2.2 Electrochemistry

Electrochemical test can quickly evaluate the influence of environmental factors on the corrosion performance. In order to study the corrosion performance of 7N01-T4 aluminum alloy, Potentiodynamic Polarization Measurement was carried out at the scanning rate of 1 mV/s. Each sample was tested three times, and the average value of electrochemical parameters obtained three times was taken as the final result. The test environment was room temperature and the medium was 3.5 wt% NaCl solution. Polarization test was carried out on CS2000 electrochemical workstation, in which three-electrode system was used for polarization test and the working electrode was connected to the test sample by wire. The sample of base metal and weld area was cut by electric spark wire cutting to a size of  $5 \times 5$  mm<sup>2</sup>. All surfaces except test surfaces shall be sealed with denture powder after welding wires. After polishing the test surface according to the metallographic sample preparation procedure, it was cleaned with anhydrous ethanol to remove oil and water stains on the surface, and dried for later use. The scanning potential range was relative open circuit potential ±0.5 V, and the scanning rate was 1 mV/s.

Table 1: Main chemical composition of 7N01 aluminum alloy and ER5356 welding wire (wt%)

Material	Si	Fe	Cu	Mn	Mg	Zn	Ti	Al
7N01	0.061	0.009	0.096	0.307	1.114	4.38	0.058	Residual volume
ER5356	0.25	0.10	0.10	0.10	4.6	0.10	0.20	Residual volume

Table 2: Laser-arc composite welding process parameters

Parameter	Laser power (kW)	Welding speed (mm/s)	Wire feeding speed (m/min)	Shielding gas	Butt joint gap (mm)	Defocusing amount (mm)
Numerical value	4	10	8.5	Ar	0.2	0

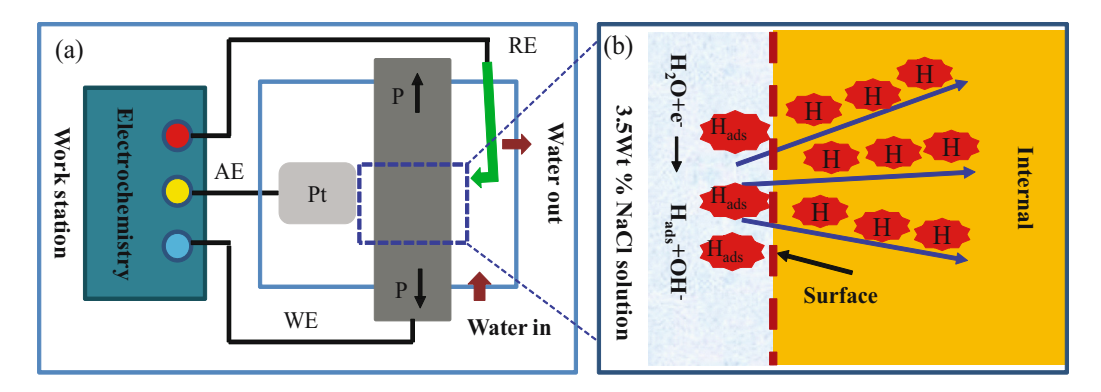


Figure 1: Schematic diagram of test design: (a) synchronously applied cathode potential of SSRT test and (b) hydrogen atoms adsorbed on the surface of the material and diffusing into the material under the action of cathode potential.

## 2.3 Slow strain rate tensile test (SSRT)

The sensitivity of 7N01-T4 laser-arc composite welded joints to hydrogen stress corrosion was evaluated by SSRT test. The reference standard is *GB/T15970.7-2000 Corrosion of Metals and Alloys – Stress Corrosion – Part 7: Slow Strain Rate Test.* SSRT samples of base metal and joint are taken perpendicular to the welding direction. The length of SSRT sample is 25 mm, and the thickness is 3 mm. MTS-300 tensile testing machine was used for SSRT test.

SSRT tests were carried out in 3.5 wt % NaCl solution at 25°C and strain rate set at  $10^{-6}~\rm s^{-1}$ . The cathode potential was applied through the CS2000 electrochemical workstation. The sample was used as the working electrode, saturated calomel electrode as the reference electrode, and platinum electrode as the auxiliary electrode, as shown in Figure 1(a). When the cathode potential is applied during the SSRT test, "hydrogen evolution reaction" will occur on the sample surface, and hydrogen atoms can be adsorbed on the sample surface and gradually diffuse into the sample, as shown in Figure 1(b). After the SSRT test, the fracture surface morphology of the sample was observed and analyzed under scanning electron microscope.

## 3 Results and discussion

#### 3.1 Polarization curve

Figure 2 shows the polarization curve of 7N01-T4 aluminum alloy base metal and joint weld in 3.5% NaCl solution (scanning rate is  $1\,\text{mV/s}$ ). In electrochemical corrosion, the corrosion resistance of metal materials can be evaluated by self-corrosion potential. Generally

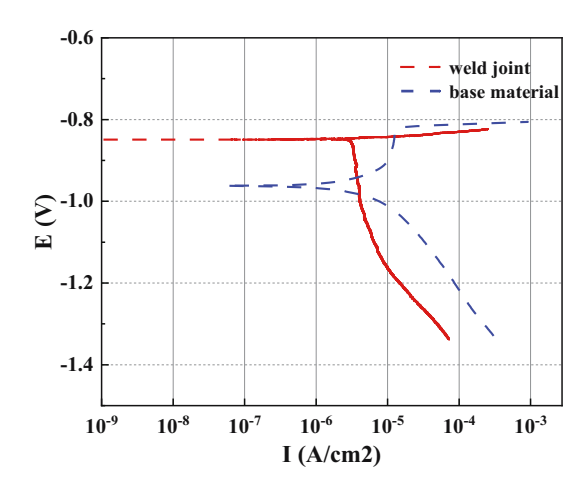


Figure 2: Polarization curves of 7N01-T4 aluminum alloy base metal and joint weld zone.

speaking, the greater the self-corrosion potential is, the better its corrosion resistance is, and *vice versa*. Therefore, it can be obviously found from Figure 2 that the self-corrosion potential of weld is higher and the self-corrosion potential of base metal is lower, indicating that the weld has better corrosion resistance. The reason for the good corrosion resistance of the weld is that the filler material is ER5356 welding wire, and the alloy is Al–Mg, which has good corrosion resistance [16].

According to the test results, it can be found that the corrosion potential of base metal and weld is basically in the range of -0.8 to -1.4 V. Therefore, the potentials of -0.8, -1.0, -1.2, and -1.4 V were selected as the cathodic potentials applied in the subsequent SSRT hydrogen stress corrosion tests.

Polarization curve analysis shows that the weld self-corrosion potential is higher and the base metal self-corrosion potential is lower, indicating that the weld has better corrosion resistance. The reason for the good

corrosion resistance of the weld is that the filler material is ER5356 welding wire, and the alloy is Al–Mg, which has good corrosion resistance.

#### **3.2 SSRT**

Figure 3 shows the SSRT stress-strain curves of base metal and joint under the condition of potentiostatic polarization in 3.5 wt% NaCl solution at room temperature. It can be seen from Figure 3 that the slope of stressstrain curves of base material and joint samples at elastic deformation stage is almost the same under different potentiostatic polarization conditions, indicating that potentiostatic polarization has no obvious influence on the elastic deformation behavior of base material and joint. In addition, the overall tensile strength and elongation of the base metal are better than that of the welded joint, mainly because of the performance of the weld. The performance of the weld is related to the chemical composition. fusion ratio, and crystallization process of the filler wire. The weld area is mainly the as-cast structure formed by the solidification of Al-Mg welding wire after melting, resulting in low mechanical properties of the weld. Generally, the as-cast grain size is coarse. According to the Hall-Petch formula, the smaller the grain size is, the greater the yield strength is ref. [17]. Therefore, the yield strength of the weld is lower than that of the base metal, which is also the reason for the low weld strength. On the other hand, the aluminum alloy laser-arc composite welding process will inevitably produce small pores and other defects, and these defects will become the stress concentration

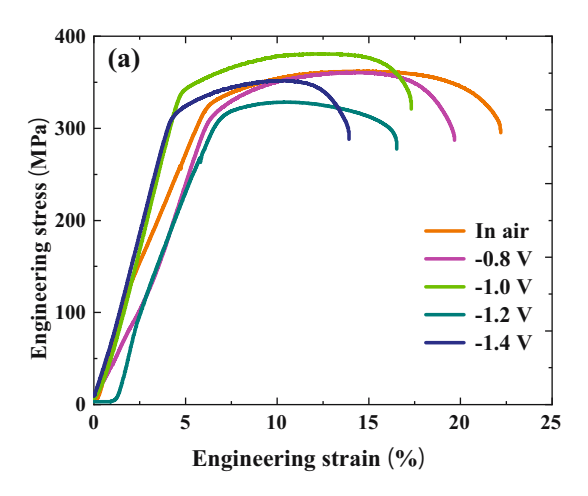
position under the action of external tensile force, leading to the joint fracture in advance, resulting in low welding joint fracture strength.

In addition, the same rule can be found in the engineering stress-strain curves of the base metal and the joint, that is, the base metal and the joint have the best tensile properties (breaking strength and elongation are the best) in the air environment. With the increase in the applied cathode potential, the tensile properties of both the base metal and the joint decrease, and the more negative the cathode potential shifts, the worse the fracture resistance. The reason is that when cathode potential is applied to aluminum alloy material, the material indicates that hydrogen evolution reaction will occur, and the reaction intensity increases gradually with the negative shift of the applied potential [18,19]. At this point, hydrogen, driven by external stress and internal stress, will migrate and enrich toward hydrogen trap areas such as grain boundaries, phase boundaries, dislocation, and pores, resulting in hydrogen-induced stress cracking of the material [20,21].

According to the above SSRT tensile test results, stress corrosion sensitivity index  $I_{\rm SSRT}$  was used for quantitative comparative analysis of stress corrosion sensitivity of the base metal and joint.  $I_{\rm SSRT}$  calculation formula (1) is as follows:

$$I_{\text{SSRT}} = 1 - \frac{\sigma_{\text{fw}} \times (1 + \delta_{\text{fw}})}{\sigma_{\text{fA}} \times (1 + \delta_{\text{fA}})}, \tag{1}$$

where  $\sigma_{\rm fw}$  is the breaking strength in corrosive environment,  $\delta_{\rm fw}$  is the elongation after break in corrosive environment,  $\sigma_{\rm fA}$  is the breaking strength in air, and  $\delta_{\rm fA}$  is the elongation after break in air.



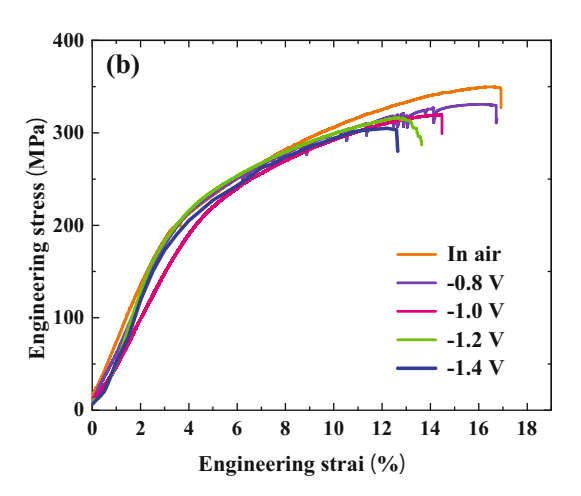


**Figure 3:** SSRT tensile test results: (a) engineering stress—strain curve of the base metal and (b) engineering stress—strain curve of 7NO1-T4 welded joint.

According to formula (1), the engineering stress–strain curves of the base metal and joint were extracted, sorted, and analyzed to obtain the values of various parameters required for the calculation of stress sensitivity index as shown in Table 3. Finally, the stress sensitivity index value  $I_{\rm SSRT}$  of the base metal and joint under different cathode potentials was obtained through comprehensive calculation.

Based on the data calculated in Table 3, the corresponding relation curve between the cathode potential applied by the base material and the joint and the stress sensitivity index were drawn, as shown in Figure 4. As can be seen from Figure 4, the overall curve of the base metal is higher than that of the joint, indicating that the stress sensitivity index of the base metal is higher than that of the joint, and the base metal has a higher stress corrosion sensitivity tendency. Generally speaking, the higher the stress sensitivity index is, the worse the stress corrosion resistance will be. Therefore, compared with the base metal, the laser-arc composite welded joint of 7N01-T4 aluminum alloy has better stress corrosion resistance [22].

In addition, with the negative shift of the applied cathode potential, the base metal and the joint have the same change trend, and the stress sensitivity index  $I_{\rm SSRT}$  of the two gradually rises to the maximum value. This also confirms the above analysis that negative cathode potential shift results in intensified hydrogen evolution reaction [23]. As the applied cathode potential increases, the  $I_{\rm SSRT}$  index is lowest at the cathode potential of  $-0.8~\rm V$ , 0.114 for the base material and 0.058 for the joint. The joint has such a low stress sensitivity index that there is almost no stress corrosion tendency at this potential. Then, with the negative potential shift, the stress index increases gradually. When it reaches  $-1.4~\rm V$ , it has the maximum  $I_{\rm SSRT}$  index value, which is 0.430 for the base metal and 0.337 for the joint.

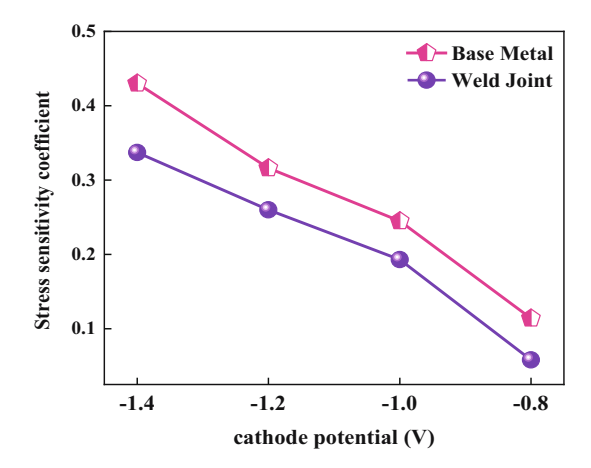


Figure 4: Polarization curves of 7N01-T4 aluminum alloy base metal and joint weld zone.

It can be drawn that the overall curve of the base metal is higher than that of the joint, indicating that the base metal has a higher stress corrosion sensitivity index than that of the joint, and the base metal has a higher stress corrosion sensitivity tendency. Therefore, compared with the base metal, 7N01-T4 aluminum alloy laser-arc composite welded joint has better stress corrosion resistance.

## 3.3 Fracture morphology

Typical tensile fracture at slow tensile rate was selected to study the stress corrosion fracture characteristics of the base metal and welded joint by observing and analyzing the fracture morphology of base metal and welded joint in air environment and 3.5 wt% NaCl corrosion environment. Figure 5 shows the fracture morphology characteristics of base metal in air environment and at various cathode potentials. Figure 6 shows the microstructure

Table 3: Stress corrosion sensitivity index calculated values of each parameter

Object	Condition	$\sigma_{\sf fA}~(\sf MPa)$	$\sigma_{\sf fw}$ (MPa)	<b>δ</b> <sub>fA</sub> (%)	<b>δ</b> <sub>fw</sub> (%)	I <sub>SSRT</sub>
Base metal	Air	362	_	22.2	_	_
	-0.8 V	_	360	_	19.68	0.114
	-1.0 V	_	345	_	17.38	0.245
	-1.2 V	_	328	_	16.52	0.316
	-1.4 V	_	321	_	13.92	0.430
Welded joint	Air	349	_	16.92	_	_
	-0.8 V	_	330	_	16.85	0.058
	-1.0 V	_	326	_	14.48	0.193
	-1.2 V	_	316	_	13.64	0.260
	-1.4 V	_	305	_	12.60	0.337

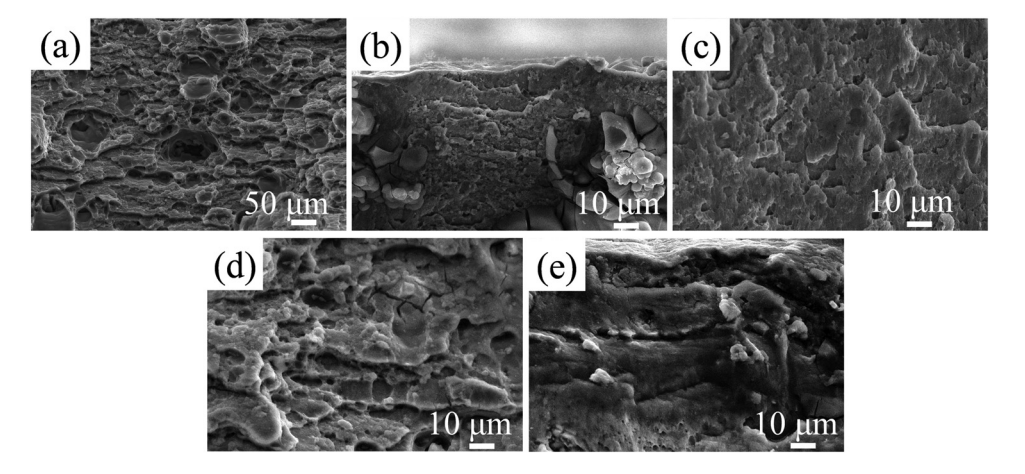


Figure 5: Microstructure of base metal fracture: (a) in air condition, (b) in the condition of cathode potential of  $-0.8 \, \text{V}$ , (c) in the condition of cathode potential of  $-1.2 \, \text{V}$ , and (e) in the condition of cathode potential of  $-1.4 \, \text{V}$ .

characteristics of 7N01-T4 welded joint in air environment and at applied cathode potentials.

It can be seen that the fracture morphology of base metal in non-corrosive media is mainly strip-shaped dimple (Figure 5(a)), indicating that it is ductile fracture. Under the action of corrosion solution and cathode potential, the surface of the fracture showed corrosion characteristics (Figure 5(b–e)). Clusters of corrosion products and mud-like patterns can be found on the surface of the fracture side (Figure 5(b)). Local intergranular fracture morphology can also be found on the surface of the fracture side, with local intergranular cracks (Figure 5(d)) and obvious layered intergranular cracks (Figure 5(e)).

In addition, the fracture positions of welded joints are all located in the weld zone. The fracture morphology of the joint in air is typical of ductile fracture, and the dimple distribution is fine and uniform (Figure 6(a)). Similar to the fracture morphology of the base metal, the fracture surface of the joint also shows corrosion characteristics due to the action of corrosive medium and applied potential (Figure 6(b and c)). At the same time, obvious intergranular fracture characteristics can be found on the surface of the fracture side, and rocky cracking morphology appears in local areas (Figure 6(d and e)).

Many experimental studies show that SCC of 7XXX series high-strength aluminum alloy mainly belongs to the hydrogen-induced cracking mechanism [24–26]. According to the hydrogen embrittlement theory, free atomic hydrogen generated in the corrosion process or self-absorbed hydrogen diffuses into the crack tip region along the grain boundary under the action of tensile stress, weakening the grain boundary and causing hydrogen embrittlement, thus

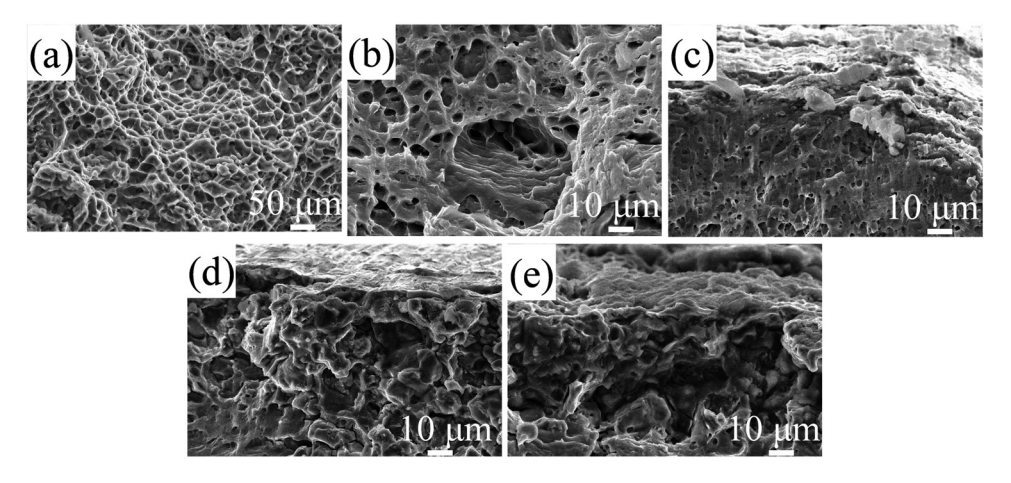


Figure 6: Microstructures of K4648 alloy after solid solution treatment: (a) in air condition, (b) in the condition of cathode potential of  $-0.8 \, \text{V}$ , (c) in the condition of cathode potential of  $-1.2 \, \text{V}$ , and (e) in the condition of cathode potential of  $-1.4 \, \text{V}$ .

accelerating the crack propagation and fracture [27–29]. Under the action of hydrogen-induced corrosion cracking, the formation of cracks starts from spot corrosion [20]. Pitting corrosion occurs because in chloride solution, the passivation film is broken by chloride ions, which induces pitting corrosion in local areas and leads to cracks [1,29–31]. We know that the reaction of aluminum alloy with water is Al +  $3H_2O = Al_3O_2 + 6H^+ + 6e^-$ . As the aluminum alloy is in 3.5 wt% NaCl solution, there will be corresponding chemical reactions at the crack tip: Al + Cl<sup>-</sup> = AlCl<sub>3</sub> +  $3e^-$  and  $Al^{3+} + H_2O = Al(OH)^{2+} + H^+$ .

In addition, under the action of applied stress, there is a great stress concentration at the crack tip. The formula (2) of the stress field of crystal crack tip is as follows:

$$\sigma_{yy} = \frac{K_i}{\sqrt{\pi \rho_0}},\tag{2}$$

where  $\sigma_{yy}$  is the stress value of the crystal crack tip,  $K_i$  is the applied load,  $\rho_0$  is the notch curvature of the crystal crack tip, which is generally considered to be equal to 2–3, and b is the crystal lattice constant. It can be found that the larger the loading load is, the more easily the stress concentration is formed in the front edge of the crack tip, and the larger the load is, the more easily the stress cracking occurs.

Under the joint action of stress field and hydrogen ion, hydrogen will gradually open the crack. The applied stress facilitates the exchange of hydrogen between aluminum alloy and corrosion environment and promotes hydrogen diffusion along grain boundaries. In addition, hydrogen can greatly reduce the bonding strength at grain boundaries, leading to the weakening of grain boundaries, resulting in grain embrittlement and intergranular cracks, resulting in grain boundary cracking and finally collapse.

In summary, observation and analysis of the fracture surface microstructure of the base metal and welded joint of 7N01-T4 aluminum alloy show that the fracture surface morphology of the base metal and welded joint is mainly a large area of dimple distribution in the non-corrosive medium environment, which belongs to the ductile fracture. Under the action of 3.5 wt% NaCl solution and applied cathode potential, the fracture characteristics of the base metal and joint changed, and corrosion traces appeared. Clusters of corrosion products and mud-like patterns were found on the surface of the fracture, and the characteristics of rock intergranular cracking appeared in some areas.

## 3.4 Stress corrosion crack propagation

Figure 7 shows the stress corrosion crack propagation path of the base metal 7N01-T4 aluminum alloy tested by EBSD. It can be seen from Figure 7(a) that the stress corrosion crack propagation path is discontinuous, and the crack at grain boundary has not been connected with the main crack, presenting a mixed fracture mechanism of transgranular and intergranular. The prefabricated crack of the sample just stays in the grain of the aluminum alloy, inside which the stress corrosion crack starts to propagate. The aluminum alloy matrix at the crack tip is constantly dissolved, and accompanying with the crack propagates through the grain with the diffusion and aggregation of hydrogen.

Generally, the large angle grain boundary is the position of strong trap for hydrogen, whose formation reduces the mobility of hydrogen atoms, which continue to gather and compound into hydrogen molecules, resulting in hydrogen pressure and cracks fracturing along the grain

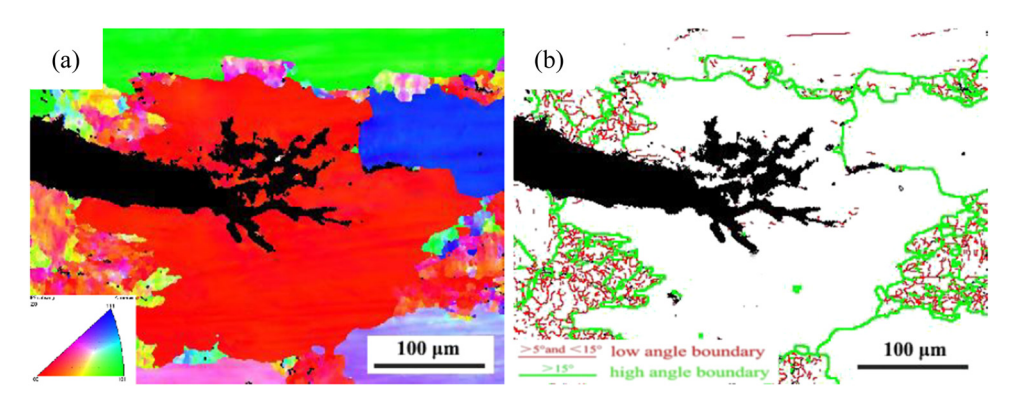


Figure 7: Stress corrosion crack propagation path of 7N01-T4 aluminum alloy: (a) stress corrosion crack propagation path of base metal 7N01-T4 aluminum alloy and (b) cracks crack path along grain boundary.

boundary, as shown in Figure 7(b). Meanwhile, it shows rock sugar pattern and intergranular secondary crack on the fracture surface, and the existence of micropores and hairlines on grain boundaries proves that SCC is related to hydrogen embrittlement. At the same time, small and shallow dimples without inclusions appeared on the crystal plane of the sample fracture, reflecting the deterioration of the toughness of the material. That is because the dimples were formed by hydrogen aggregation rather than ductile fracture. According to the theory of fracture mechanics, the cracks in the middle of the sample are in plane strain state, which is conducive to hydrogen enrichment, which is one of the reasons for the long cracks in the middle of sample. In addition, the stress corrosion crack propagation zone of heat affected zone and base material sample is relatively clean and no corrosion products are attached, also presenting the feature of hydrogen-induced crack fracture.

#### 4 Conclusion

This work studied the hydrogen-induced stress corrosion of 7N01-T4 aluminum alloy for railway vehicles by combination of potentiodynamic polarization measurement and slow strain rate tensile test. Polarization curve analysis shows that the weld self-corrosion potential is higher and the base metal self-corrosion potential is lower, indicating that the weld has better corrosion resistance. In addition, it can be drawn that the fracture morphology of base metal and joint in non-corrosive medium is mainly large area dimple distribution, which belongs to ductile fracture. Clusters of corrosion products and mud-like patterns were found on the surface of the fracture, and the characteristics of rock intergranular cracking appeared in some areas. The above conclusions could provide some reference for investigating the cause and mechanism of hydrogen-induced stress corrosion of 7N01-T4 aluminum alloy and other similar materials, providing greater security for the safety of railway vehicles.

**Acknowledgments:** This work was supported by Study on Stress Corrosion Process Control and Life Evaluation Technology of High-strength Aluminum Alloy Used in Rail Transit Vehicles Project No. CIJS21-kj030 from CRRC.

**Funding information:** Project name: Study on Stress Corrosion Process Control and Life Evaluation Technology of High-strength Aluminum Alloy Used in Rail Transit Vehicles. Project No. CIJS21-kj030 from CRRC.

**Author contributions:** Zhang Li-jiao: conception, experiment, measurement, and drafting of original manuscript. Li Ming-gao: Project administration, theory, formula, and editing of manuscript.

**Conflict of interest:** The authors declare that they have no known competing financial interests or personal relationships that could have appeared to influence the work reported in this article.

## Reference

- [1] Boinovich, L., A. Emelyanenko, A. Modestov, A. Domantovsky, A. Shiryaev, K. Emelyanenko, et al. Corrosion behavior of superhydrophobic aluminum alloy in concentrated potassium halide solutions: when the specific anion effect is manifested. *Corrosion Science*, Vol. 112, 2016, pp. 517–527.
- [2] Wang, X. M., G. Q. Gou, J. J. Zhao, and Y. Liu. Study on the intergranular corrosion behavior of welding joint of A7N01-T4 Al-Alloy for high-speed train. *Advanced Materials Research*, Vol. 284–286, 2011, pp. 1594–1597.
- [3] Qin, C., G. Gou, X. Che, H. Chen, J. Chen, P. Li, et al. Effect of composition on tensile properties and fracture toughness of Al-Zn-Mg alloy (A7N01S-T5) used in high speed trains. *Materials & Design*, Vol. 91, 2016, pp. 278-285.
- [4] Gou, G., J. Chen, Z. Wang, H. Chen, C. Ma, and P. Li. Stress corrosion cracking behavior of 4.19% Zn-1.34% Mg (A7N01S-T5) aluminum alloy welded joints. *Corrosion*, Vol. 72, No. 9, 2016, pp. 1133–1145.
- [5] Yan, D. J., X. S. Liu, L. I. Jun, J. G. Yang, and H. Y. Fang. Effect of strain hardening and strain softening on welding distortion and residual stress of A7N01-T4 aluminum alloy by simulation analysis. *Journal of Central South University: English Edition*, Vol. 17, No. 4, 2010, id. 8.
- [6] Li, S., H. Dong, L. Shi, P. Li, and F. Ye. Corrosion behavior and mechanical properties of Al-Zn-Mg aluminum alloy weld. *Corrosion Science*, Vol. 123, 2017, pp. 243–255.
- [7] Wang, S., B. Luo, Z. Bai, Y. Zheng, C. He, and G. Jiang. Revealing the aging time on the precipitation process and stress corrosion properties of 7N01 aluminium alloy. *Vacuum*, Vol. 176, 2020, id. 109311.
- [8] Cavanaugh, M., N. Birbilis, and R. Buchheit. Modeling pit initiation rate as a function of environment for Aluminum alloy 7075-T651. *Electrochimica Acta*, Vol. 59, 2012, pp. 336–345.
- [9] Gupta, R. K., A. Deschamps, M. K. Cavanaugh, S. P. Lynch, and N. Birbilis. Relating the early evolution of microstructure with the electrochemical response and mechanical performance of a Cu-rich and Cu-lean 7xxx aluminum alloy. *Journal of The Electrochemical Society*, Vol. 159, No. 11, 2012, id. C492.
- [10] Ma, C., G. Kang, G. Gou, H. Chen, and X. Che. Effect of charging hydrogen on the tensile properties of A7N01 aluminum alloy friction stir welded joints. *International Journal of Modern Physics B*, Vol. 33, No. 01–03, 2019, id. 1940043.
- [11] Shen, L., H. Chen, L. D. Xu, X. L. Che, and Y. Chen. Stress corrosion cracking and corrosion fatigue cracking behavior of

- A7N01P-T4 aluminum alloy. Materials and Corrosion, Vol. 69, No. 2, 2018, pp. 207-214.
- [12] Jr. Yokobori, A. T., Y. Chinda, T. Nemoto, K. Satoh, and T. Yamada. The characteristics of hydrogen diffusion and concentration around a crack tip concerned with hydrogen embrittlement. Corrosion Science, Vol. 44, No. 3, 2002, pp. 407-424.
- [13] Qi, W., R. Song, X. Qi, H. Li, Z. Wang, C. Wang, et al. Hydrogen embrittlement susceptibility and hydrogen-induced additive stress of 7050 aluminum alloy under various aging states. Journal of Materials Engineering and Performance, Vol. 24, No. 9, 2015, pp. 3343-3355.
- [14] Akbari, M., P. Asadi, P. Zolghadr, and A. Khalkhali. Multicriteria optimization of mechanical properties of aluminum composites reinforced with different reinforcing particles type. ARCHIVE Proceedings of the Institution of Mechanical Engineers Part E Journal of Process Mechanical Engineering, Vol. 232, No. 3, 2018, pp. 323-337.
- [15] Akbari, M. and P. Asadi. Simulation and experimental investigation of multi-walled carbon nanotubes/aluminum composite fabrication using friction stir processing. Proceedings of the Institution of Mechanical Engineers, Part E: Journal of Process Mechanical Engineering, Vol. 235, No. 6, 2021, id. 2165.
- [16] McMahon, M. E., J. R. Scully, and J. T. Burns. Mitigation of intergranular stress corrosion cracking in Al-Mg by electrochemical potential control. JOM, Vol. 69, No. 8, 2017, pp. 1389-1397.
- [17] Zhou, D., H. Wang, D. W. Saxey, O. Muránsky, and D. Zhang. Hall-petch slope in ultrafine grained Al-Mg alloys. Metallurgical and Materials Transactions A, Vol. 50, No. 9, 2019, pp. 4047-4057.
- [18] Ma, H., Z. Liu, C. Du, H. Wang, C. Li, and X. Li. Effect of cathodic potentials on the SCC behavior of E690 steel in simulated seawater. Materials Science & Engineering A, Vol. 642, 2015,
- [19] Wang, W. W., J. Luo, L. C. Guo, Z. M. Guo, and Y. J. Su. Finite element analysis of stress corrosion cracking for copper in an ammoniacal solution. Rare Metals, Vol. 34, No. 6, 2015, pp. 426-430.
- [20] Li, L., S. Bo, Z. Cai, L. Zhen, and X. Cui. Effect of vanadium content on hydrogen diffusion behaviors and hydrogen induced ductility loss of X80 pipeline steel. Materials Science and Engineering A, Vol. 742, 2019, pp. 712-721.

- [21] Zhfa, B., A. Tl, A. Mls, A. Gqg, A. Zyz, A. Cpm, et al. Hydrogen atoms on the SCC behavior of SUS301L-MT stainless steel laser-arc hybrid welded joints. Corrosion Science, Vol. 148, 2019, pp. 272-280.
- [22] Costa, D., T. Ribeiro, P. Cornette, and P. Marcus. DFT modelling of corrosion inhibition by organic molecules: carboxylates as inhibitors of aluminium corrosion. Journal of Physical Chemistry C, Vol. 120, No. 50, 2016, pp. 28607-28616.
- [23] Chen, Z., Y. Nong, J. Chen, Y. Chen, and B. Yu. A DFT study on corrosion mechanism of steel bar under water-oxygen interaction. Computational Materials Science, Vol. 171, 2020, id. 109265.
- [24] Rao, A., V. Vasu, M. Govindaraju, and K. Srinadh. Stress corrosion cracking behaviour of 7xxx aluminum alloys: A literature review. Transactions of Nonferrous Metals Society of China, Vol. 26, No. 6, 2016, pp. 1447-1471.
- [25] Zheng, C. B., B. H. Yan, K. Zhang, and G. Yi. Electrochemical investigation on the hydrogen permeation behavior of 7075-T6 Al alloy and its influence on stress corrosion cracking. International Journal of Minerals Metallurgy and Materials, Vol. 22, No. 7, 2015, pp. 729-737.
- [26] Sun, X. Y., B. Zhang, H. Q. Lin, Y. Zhou, L. Sun, J. Q. Wang, et al. Correlations between stress corrosion cracking susceptibility and grain boundary microstructures for an Al-Zn-Mg alloy. Corrosion Science, Vol. 77, 2013, pp. 103-112.
- [27] Qi, X., R. Song, W. Qi, J. Jin, C. Wang, H. Li, et al. Correspondence between susceptibility to SCC of 7050 aluminum alloy and passive film-induced stress at various pH values. Journal of Wuhan University of Technology-Mater Sci Ed, Vol. 32, No. 1, 2017, pp. 173-178.
- [28] Borchers, T. E., D. P. McAllister, and W. Zhang. Macroscopic segregation and stress corrosion cracking in 7xxx series aluminum alloy arc welds. Metallurgical & Materials Transactions A, Vol. 32, 2015, pp. 1827-1833.
- [29] Borchers, T. E., A. Seid, P. Shafer, and W. Zhang. Exacerbated stress corrosion cracking in arc welds of 7xxx aluminum alloys. Welding in the World, Vol. 62, No. 4, 2018, pp. 783-792.
- [30] Tian, W., S. Li, B. Wang, J. Liu, and M. Yu. Pitting corrosion of naturally aged AA 7075 aluminum alloys with bimodal grain size. Corrosion Science, Vol. 113, 2016, pp. 1-16.
- [31] Beeri, O., S. I. Baik, A. I. Bram, M. Shandalov, D. N. Seidman, D. C. Dunand. Effect of U and Th trace additions on the precipitation strengthening of Al-0.09Sc (at.%) alloy. Journal of Materials Science, Vol. 54, No. 4, 2019, pp. 3485-3495.